

## Chapter 2

# **Mechanical Characterization of Released Thin Films by Contact Loading**

## **2.1 Introduction**

The design of reliable and functional micro/nano electro mechanical systems (MEMS/NEMS) relies on the knowledge and understanding of the mechanical behavior of their materials [1-3]. Due to surface effect and grain size, the material properties may not be the same as the bulk material. Moreover, the manufacturing processes such as etching, temperature, and humidity affect the material properties significantly. For these reasons, the on chip testing is desired for MEMS devices to obtain the properties. Meanwhile, it is desirable to be able to test each device individually and protect the untested devices on the same chip/wafer as the tested sample.

The trend to reduce the dimensions of the MEMS devices' structures such as free standing thin films, membranes, and cantilevers, warrants load and displacement sensitivity in the sub-mN and sub- $\mu\text{m}$  scales. For typical metal or ceramic materials in the sub-mm geometric dimension of MEMS devices, the required load is in the range of from 1 mN to 1N, and the displacement measurement is in the range of 1  $\mu\text{m}$  to 100  $\mu\text{m}$ . These requirements cannot be satisfied by the traditional mechanical characterization tools such as MTS and Instron instruments. On the other hand, nano-indentation systems, which work

in pico- to nano-Newton loading range and sub-micron displacement range are suitable for local characterization but not sufficient for micro device characterization. Therefore, there is a great interest in developing new techniques that allows testing in the gap between the capabilities of these two well-established methods.

Recently, many efforts on new testing methods were made by different research groups to explore the mechanical properties on free standing thin films [4-16]. A wide variety of new methods for testing the mechanical behavior of thin free standing specimens has been developed. These methods typically impose a fixed displacement by means of a nano-positioning motor [9-15] or an on-chip actuator [16] and measure the load. Displacement-control experiments are suitable for large specimens and/or for ductile materials, which exhibit relatively high fracture toughness. However, the fragile nature and the nonlinear behavior of part of the MEMS structures raise the possibility to have a transient load, which may cause failure under displacement control. Therefore, it is desirable to test fragile MEMS structures in a load-control instrument, i.e., an instrument that imposes a force and measure the displacement. Displacement-control instruments can be adapted for load control by means of a feedback loop. But, there are severe limits on the response time and this is effective only for quasi-static tests instead of dynamic testing. Further, the possibility to have large undesired transient load still exists. Therefore, it is demanding to develop new techniques, which operate under load control nature for measuring mechanical properties of fragile MEMS devices.

Moreover, part of the MEMS structures can be studied only by dynamic load controlled experiments. These include micro-actuators, which are evaluated by the load they can

overcome, and active materials such as shape memory alloys, electrostrictive, and magnetostrictive materials, in which the load (i.e., the stress and not the strain) determines the driving force for microstructural changes such as domain switching. These advanced functional devices require being studied under a combination of a controlled-load and a dynamic electric/magnetic/thermal loading. Such experiments are currently beyond the scope of existing techniques.

In this chapter, a new technique is presented for measuring the static and dynamic mechanical response of free standing thin film MEMS structures under load control. The developed apparatus consists of inexpensive off-the-shelf products and can be used for dynamic electro/magneto/thermo mechanical characterization experiments. The capabilities of the technique were demonstrated by testing the behavior of amorphous  $\text{Si}_3\text{N}_4$  membrane structures and the results demonstrated ability to avoid local or transient stress concentration during the entire experimental process.

## **2.2 Experiment**

### **2.2.1 Experimental setup**

The requirement of the loading and displacement range and as well as the fragility of the sample increase the difficulties in designing a new characterization method for MEMS devices.

The traditional methods for displacement measurement such as the strain gauge and linear variable differential transformer (LVDT) require partial or entire sensor to be directly attached on the surface whose displacement needs to be measured. These methods are

impossible to be used on the fragile sub-micron thick free-standing thin films and membranes. To overcome these difficulties, laser beam and the position sensing device (PSD) were used to avoid contacting the sample directly.

Designing an appropriate loading method is also challenging. In principle, load control can be obtained if the spring constant of the apparatus, i.e., the mechanical structure that transmits the load from the motor (or actuator) to the specimen, is significantly smaller than that of the specimen. In this situation the applied force,  $F$ , is directly determined by the displacement imposed by the motor,  $S$ , via  $F \cong K_0 S$  where  $K_0$  is the effective spring constant of the apparatus. However, this condition requires a very small  $K_0$  value, which results in a low resonant frequency of the apparatus and limits the application of dynamic experiments. In this work, this problem is overcome by applying the load via a magneto-static interaction in which the response time is much faster.

A schematic of the experimental setup is shown in figure 2.1. The load is applied by a tip, which is attached to one end of a substantially rigid beam. The force applied to the sample is proportional to the magnetostatic force being applied to the other end of the rigid beam. The later force is controlled by changing the distance between a pair of permanent magnets; one is attached to the beam and the other is attached to an external post and is able to move vertically. The upper magnet is aligned in the horizontal plane, using an X-Y micro-stage, such that it is situated exactly above the bottom magnet and no lateral forces are applied on the rigid beam.

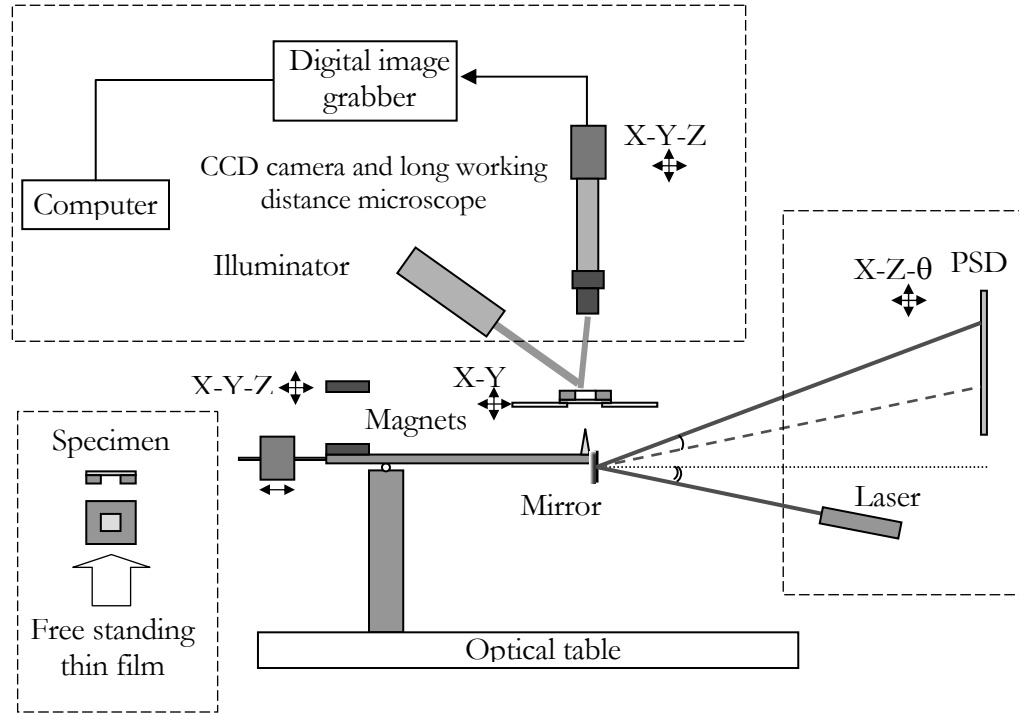


Figure 2.1. Schematic illustration of the experimental setup.

A wide variety of methods have been suggested in the literature for measuring specimen displacements (or strains) in micro-mechanical testing apparatuses. These include imaging techniques [9-12], interference patterns [13-14], diffraction spots [15], and capacitance measurements [16]. These methods are either limited by low sampling rates or not having high enough resolution for large deformation. Some of these methods need special treatment of the samples which can alter the sample structure. In order to enable dynamic experiments, the loading tip displacement which is the same as the displacement of the sample at the contact point, is measured by monitoring the deflection of a single laser beam, which is reflected from a mirror attached to the end of the rigid beam. The reflected laser beam is sensed by a Position Sensitive Detector (PSD) (Hamamatsu, S3979), which is attached to an external post, and the resulting voltage signal is recorded using an

oscilloscope (Nicolet, Model 40) (see figure 2.1). The PSD circuit allows sampling rates of up to 100 kHz and has a typical precision of about 1  $\mu\text{m}$ . A Y-Z- $\theta$  stage was designed to mount the PSD and helped with the alignment of the sensor.

In figure 2.2, the contact tip displacement is  $u$ , the horizontal distance between the mirror and PSD sensor is  $L$ , between the tip and the pivot point is  $l_0$ , the initial angle of the laser beam is  $\alpha$ . Then, the deflection angle  $\theta$  and magnified displacement  $D$ , which is measured by the PSD, satisfies the following equations:

$$\theta = u/l_0$$

$$D = 2 \cos \alpha L \theta$$

In the current setup, the parameters are fixed:  $l_0 = 10 \text{ cm}$ ,  $L = 54 \text{ cm}$ ,  $\alpha = 15^\circ$ , then the geometrical magnification is computed to be 10, i.e.,  $D \cong 10u$ .

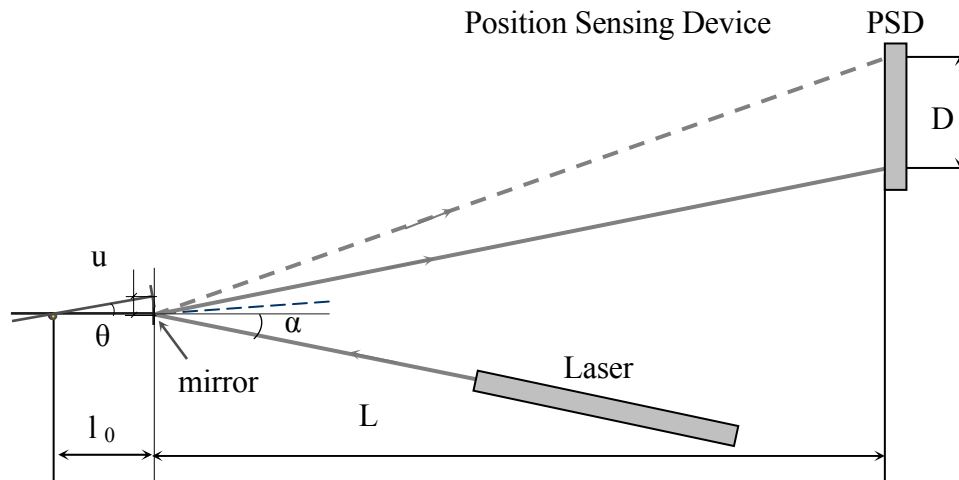


Figure 2.2. Illustration of the displacement measurement system.

Due to this geometrical amplification a typical resolution of 0.1  $\mu\text{m}$  can be obtained in the tip displacement measurement.

The sample is mounted on an X-Y-Z micro-stage and its alignment with respect to the tip is monitored by a long working distance optical microscope equipped with a CCD camera connected to a computer with digital frame grabbing hardware (EPIX Inc, PIXCI SV4) and software (EPIX Inc, XCLIBV2.2-DWT-U and XCAPLITE-WIN-V2.2).

Note that all the controlling and monitoring components, i.e., the upper magnet, the laser, the PSD, and the microscope, are isolated from the rigid beam. This fact significantly reduces the vibration and noise and protects the very fragile structures that are being tested.

The choice of the loading tips is critical in this technique since these tips are employed to apply contact loading to fragile specimens. Thin films grown by MEMS fabrication methods like MBE or CVD will have various surface roughness, in the range of 1 ~ 100 nm, depending on the fabrication process and film thickness. To reduce the local load concentration, the smoothness of the loading tip surface is critical. A wide variety of tip shapes and dimensions are commercially available, which can provide a variety of loading conditions, including point load and line load conditions. A ruby ball tip is chosen in the current setup. The tip has the required well-defined surface, and is relatively large in diameter (~ 300  $\mu\text{m}$ ) to avoid stress concentration and prevent damage to the fragile specimens of ceramic thin films. The SEM images of the loading tip in figure 2.3 shows the smooth surface of the loading tip. The largest possible tip is chosen relative to the size of the specimens studied.

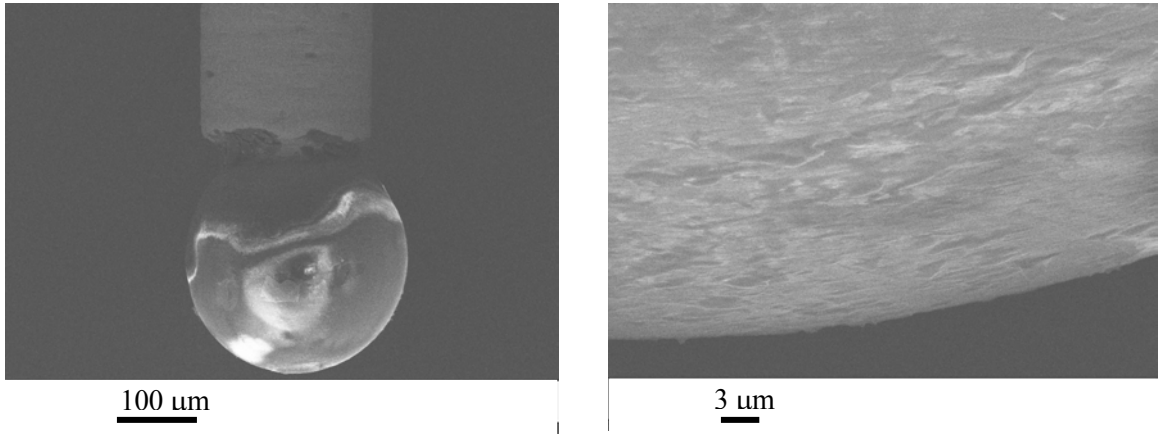


Figure 2.3. SEM image of the ruby ball tip.

The magnetostatic force is actually determined by the difference  $\Delta d = d_0 - d$ , where  $d_0$  is the initial distance between the magnets at the point where the tip first comes into contact with the sample and  $d$  is the distance between the magnets at some arbitrary moment during the experiment (see illustration in figure 2.4). The working conditions are chosen in which  $d_0 = 100$  mm and  $\Delta d$  varies in the range of up to 13 mm. Under these conditions the sample (or load cell) displacements at the  $\mu\text{m}$  scale are negligible in comparison to  $\Delta d$ , and hence  $\Delta d \cong \Delta z$ , where  $\Delta z = z_0 - z$  relates to the absolute readings of the upper magnet position (see figure 2.4). Thus, the load is determined directly by the upper magnet position and load-control conditions are achieved. Moreover, since  $d_0 \gg \Delta z$ , there is nearly a linear relation between  $F$  and  $\Delta z$  as is demonstrated by the calibration curve presented in figure 2.4, which was measured by placing an 50 g load cell (Omega, CF50g) instead of the sample. It can be deduced from the curve in figure 2.4, *left* that 1  $\mu\text{m}$  change of  $\Delta z$  results in load change of 1.5  $\mu\text{N}$ . Thus, load sensitivity in the  $\mu\text{N}$  scale can be easily obtained by moving the upper

magnet with any micro-positioning device. Note that different calibration curves, which provide different load range and different sensitivity, can be obtained by choosing different  $d_0$  values or by placing different magnets.

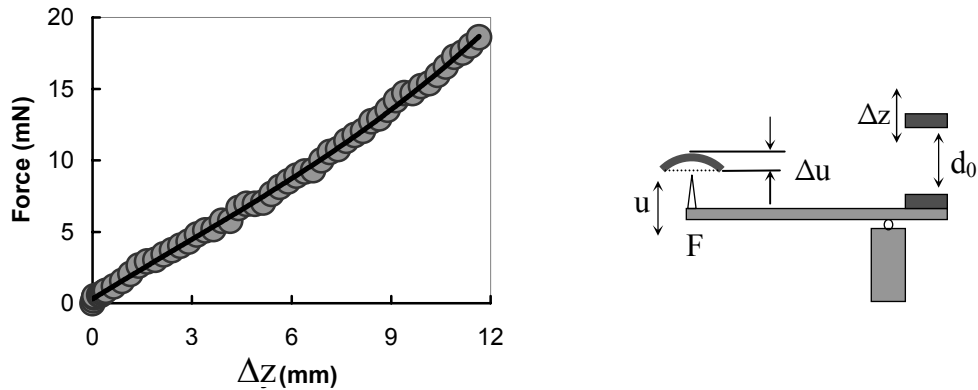


Figure 2.4. Calibration of the loading system. *Left*, calibration curve of the loading system. The applied force,  $F$  in mN, as a function of the change in the position (displacement) of the upper magnet,  $\Delta z$  in mm for the identical  $z_0$  as in the experiments. This response curve was obtained by applying force on a load cell; *right*, illustration of the geometry relations.

In principle, the sample should be placed at the same height as the load cell in order to obtain the same  $d_0$  value. Nevertheless, changes of  $d_0$  in the range of  $\pm 1$  mm results only in subtle changes of the calibration curve and hence small changes of the sample height will not have significant effect on the calibration curve. On the other hand, an accurate determination of  $z_0$ , i.e., a clear identification of the point where the tip first comes into contact with the sample, is essential in order to accurately determine  $\Delta z$ . Figure 2.5 demonstrates that  $z_0$  can be determined with an accuracy which is equivalent to the resolution of the micro-positioning device that is used to move the upper magnet. In this figure, two distinct regions are clearly observed in the plot of the tip displacement,  $u$ , as a

function of  $z$ . During the initial movement of the magnet, the tip does not touch the sample and hence its displacement is proportional to the displacement of the upper magnet and the slope is relatively large. At the point where the tip contacts the sample the slope changes abruptly, as the tip displacement is now equal to the sample displacement and is in the  $\mu\text{m}$  scale. The obvious change in slope makes it very easy to identify the contact point. The resolution of determining the contact point has the same resolution of the  $z$  measurement, i.e., the resolution on the order of  $0.1 \mu\text{m}$ . As a result, the error in contact force is on the order of sub-micro-Newton.

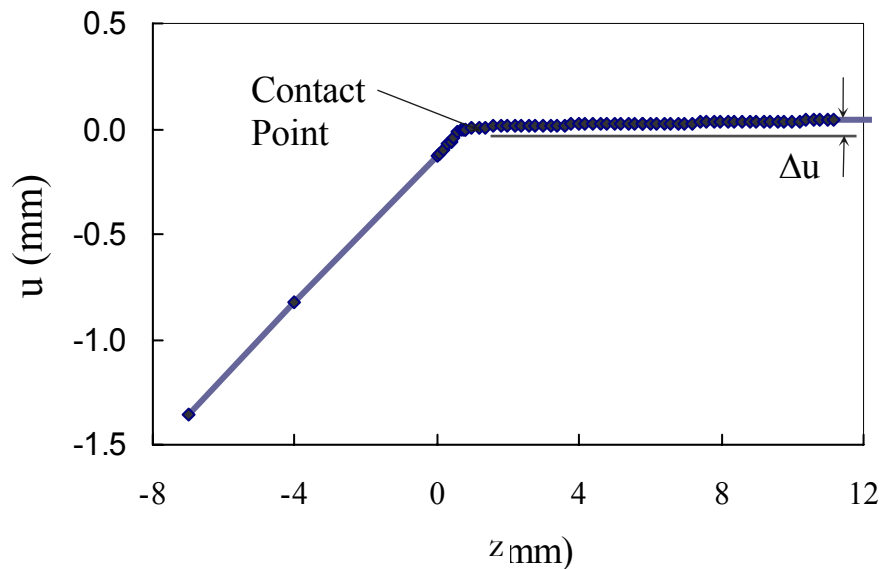


Figure 2.5. The tip displacement,  $u$ , as a function of the position of the upper magnet,  $z$ .

### 2.2.2 Material

Amorphous silicon nitride ( $\text{Si}_3\text{N}_4$ ) is widely used in MEMS industry because of its superb material chemical properties. It is also often used as an etch stop in multi-layered devices. Since it is very resilient,  $\text{Si}_3\text{N}_4$  is an ideal material for thin film growth support, such as the widely used TEM windows. MEMS devices can be grown on it with various

methods, such as MOCVD, MBE, or sol-gel method. It is also a widely-studied thin film material. Bulge tests, micro-tension tests, micro-bending tests and other methods have been performed for characterization of the Young's modulus  $E$  and other parameters of this material in free standing thin film geometry. For different deposition conditions and post processing procedures, the elastic modulus varies greatly in the range from 101 to 373 GPa [17]. For these reasons, it is an ideal material to illustrate the new technique's capability.

### 2.2.3 Results — mechanical response of $\text{Si}_3\text{N}_4$ film

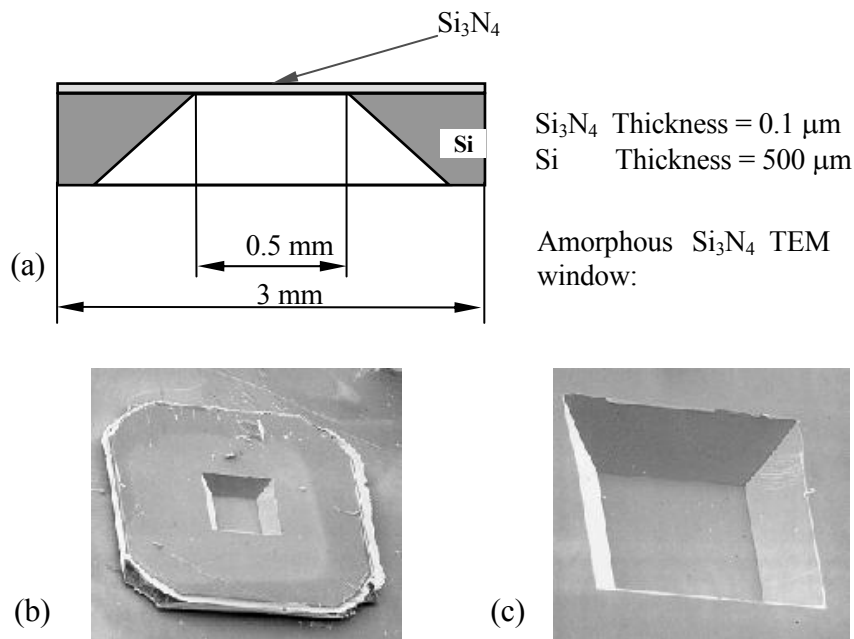


Figure 2.6. Pictures of  $\text{Si}_3\text{N}_4$  TEM window. (a) Illustration of the cross-section view of a TEM window, (b)(c) SEM images of a TEM window. (SEM images are from SPI2.com)

The capabilities of the new method are demonstrated by studying the membrane samples as shown in figure 2.6. The SEM images (from 2SPI.com) of the single TEM window are shown in figure 2.6 (b) and (c). The samples are  $0.47 \text{ mm}$  squares with  $75 \text{ nm}$  thick free standing thin films on the  $200 \mu\text{m}$  thick silicon substrate. The overall dimension

of the TEM holder is 3 x 3 mm. An array of TEM windows (figure 2.7) is also used to check the repeatability of the technique.

The membranes were produced by SPI Supplies, by depositing a  $\text{Si}_3\text{N}_4$  film on a 200  $\mu\text{m}$  thick silicon (Si) wafer and etching square windows in the Si. Note that  $\text{Si}_3\text{N}_4$  is a brittle ceramic material and that the very large ratio between the membrane's span and thickness (of about 6200) makes the mechanical structure very fragile to handle.

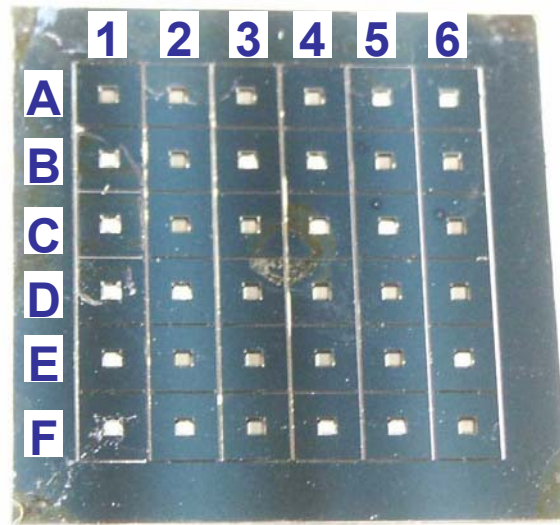


Figure 2.7. Array of TEM windows and labels of each sample.

The results presented here were taken using a ruby ball tip, having a radius of  $R = 150$   $\mu\text{m}$ . Large tip radius are desired in testing square and rectangular membranes in order to limit the indentation stress and prevent membrane rupture. As shown below, although the tip radius is a significant fraction of the membrane span, the radius of the contact region,  $r_c$ , is much smaller than the span. This fact significantly simplifies the analysis for interpretation of the data.

Figure 2.8 shows the applied force as a function of the measured tip displacement during loading and unloading processes. The two curves coincides each other with no

significant hysteresis, which means that the structure behaves elastically. The highest tip displacement is  $37.5\ \mu\text{m}$ , which is  $\sim 500$  times the film thickness. This means that the bending stresses are negligible in comparison to the stresses due to stretching, i.e., to a very good approximation the thin film behaves as a membrane.

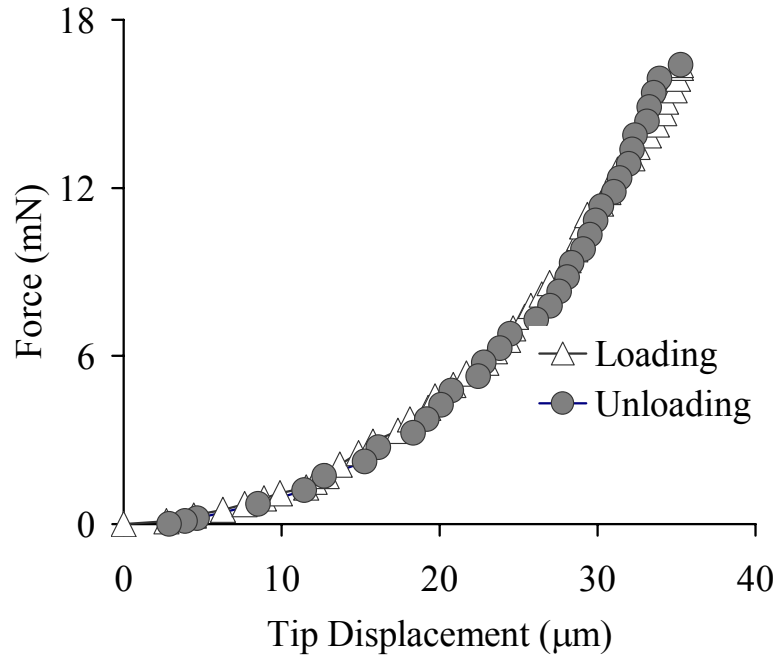


Figure 2.8. The mechanical response of a 75 nm thick free-standing amorphous silicon nitride ( $\text{Si}_3\text{N}_4$ ) film during loading and unloading.

Figure 2.9 shows a series of optical images of the membrane, which were taken under different loads. The deflected membrane forms a tent-shape where the angle of deflection,  $\theta$ , increases as the load increases. The repeatability of the new technique is demonstrated in figure 2.10, which presents the load-displacement curves of five membranes located at different regions of the same wafer. All the curves almost coincide with each other.

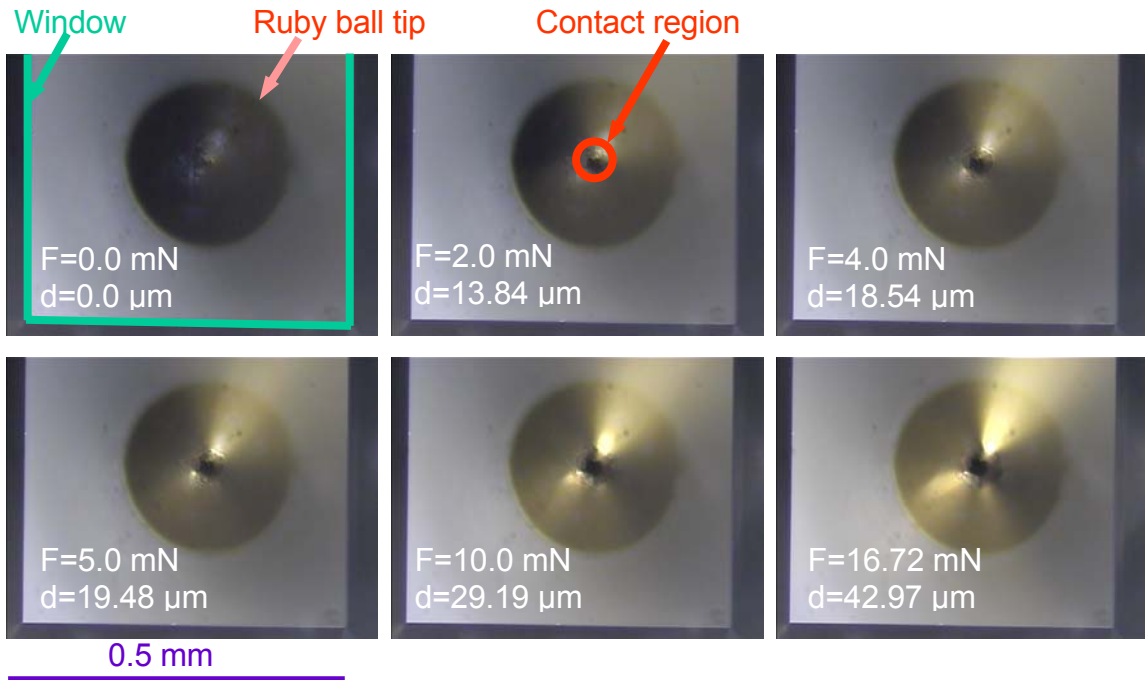


Figure 2.9. Series of optical images of membrane during loading.

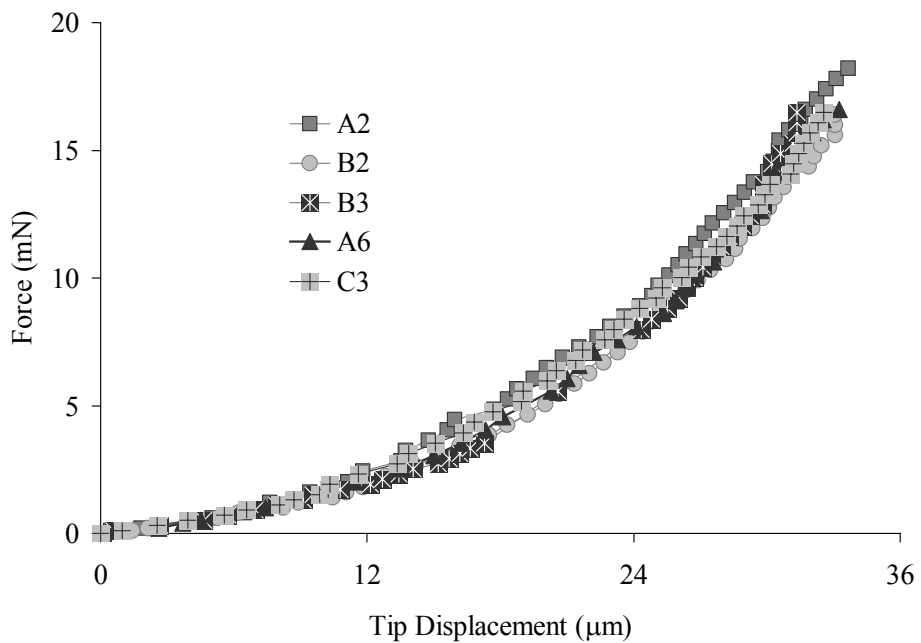


Figure 2.10. A wafer consisting of 6x6 devices (see figure 2.7) was tested at various locations. The mechanical responses of five membranes located at different regions of the same wafer are highly repeatable.

A geometrical calculation under the assumption of the membrane theory shows that the radius of the contact region is given by  $r_c = R\sin\beta$ , where  $R$  is the radius of the ruby ball tip,  $\beta$  is the thin film deflection angle. Therefore, for reasonable values of  $\beta$ ,  $r_c \ll R$  and hence  $r_c \ll a$ , where  $a$  is the span of the thin film. In these conditions the deflection angle can be assessed by  $\tan\beta = 2u/a$ . Thus, for the highest tip displacement of  $u = 37.5 \mu\text{m}$ ,  $\beta$  and  $r_c$  take values of  $10.2^\circ$  and  $26 \mu\text{m}$  respectively.

For the membrane theory approximation, the stresses at the contact region are uniform and the balance of the total forces along the  $z$ -direction yields the following expression for the membrane (stretching) stress

$$\sigma = \frac{F}{2\pi r_c \sin\beta} \cong \frac{Fa^2}{8\pi t R u^2} \quad (2.3)$$

where  $t$  is the membrane thickness, i.e., 75 nm, that of the thin film. The expression on the right hand side in Eq. (2.3) is obtained by making the small angle approximation, i.e.,  $\sin\beta \cong 2u/a$ . A substitution of the highest tip displacement,  $u = 37.5 \mu\text{m}$ , at the largest force,  $F = 16.6 \text{ mN}$ , results in membrane stress,  $\sigma = 9.2 \text{ GPa}$ .

The attainment of such high stresses and large deflections reflect the high quality, i.e., very small flaws, of the  $\text{Si}_3\text{N}_4$  membranes. This also attests to the capabilities of the developed technique to avoid local or transient stress concentrations during the entire approach, loading, and unloading phases of the experiment. This fact illustrates the capability of the new technique for studying highly fragile and micro devices and structures.

## 2.3 Modeling

The mechanical problem of contact loading by an indenter on a square membrane is very complicated. The complication is caused by two reasons. One is due to the nonlinear nature of the contact loading process. As the loads increased, the contact area changes and the maximum displacement is directly related to the shape and size of the indenter. The other reason is the large deformation associated with this problem, i.e., the non-linear effects should not be omitted in the geometrical relations. As a result, the governing equations are strongly coupled with severe non-linearity even for a simple structure as a membrane, for which the effect of bending is neglected.

For the contact problem mentioned above, Begley [18] recently investigated the axially-symmetric case and obtained a closed form solution while considering the indenter size effect. For the two-dimensional (2-D) membrane under pressure loading the solution to strongly coupled second-order partial differential equations were obtained numerically. Yet, finding analytical solutions for the combination of these two cases is still an open problem.

In the present investigation the finite element method is used to simulate this complicated mechanical problem. The indenter is simulated by a rigid sphere and the free standing film, is simulated by the same geometry as in the experimental sample, i.e., square geometry. The elastic modulus and Poisson's ratio are the unknown parameters for a thin film that remains entirely elastic during the loading. Different values are assumed for these parameters to obtain the best fit. The loading process is similar to the traditional indentation loading process, i.e., the sample is loaded by a specified indenter displacement, and the

resultant strain and stress field are obtained. In addition, the relation between the indenter load and center point displacement is obtained from the finite element analysis. In the case of thin films, the residual stress in the film is also an important parameter, which is also an unknown prior to the analysis. The values of Young's modulus ( $E$ ), Poisson's ratio ( $\nu$ ) and the residual stress ( $\sigma_0$ ) for thin film are specified within the range of expected values. The resulting load-displacement curves are fitted with the expected solution with unknown constants, which is discussed below in detail. The experimentally obtained load-displacement curves are then fitted with these constants and the unknown elastic modulus and initial stress are obtained by evaluating the best fit between the two solutions. The details of the finite element analysis, such as the modeling, meshing and boundary conditions and contact information are discussed below.

## 2.4 Finite element modeling

The geometry of the structure that is to be modeled has two parts. One is the  $470 \times 470 \times 0.1 \mu\text{m}$  thin film on a substrate, the same as the sample in the experiments. The other part is a rigid sphere with  $300 \mu\text{m}$  in diameter, the same as the indenter in the experiments.

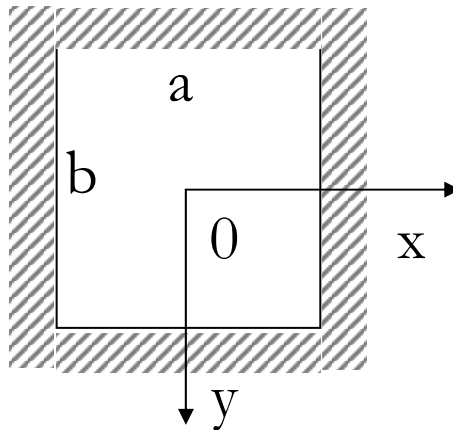


Figure 2.11. Illustration of 4 sides clamped plates.

The thin film is clamped on all four sides (figure 2.11) to simulate the boundary condition of being bonded to a rigid substrate. This corresponds to specifying both the translation and rotation of the thin film to be zero at all edges. The indenter is confined such that only translation in the  $z$  direction (normal to the thin film) is allowed. Translation in other directions and rotation in any direction are constrained for the indenter. The contact between the thin film and the spherical indenter is assumed to be frictional.

The loading is applied by specifying the axial displacement of the indenter. The pre-stress which is assumed to be equi-biaxial in  $\sigma_{xx}$  and  $\sigma_{yy}$  is added as an initial condition in the simulations.

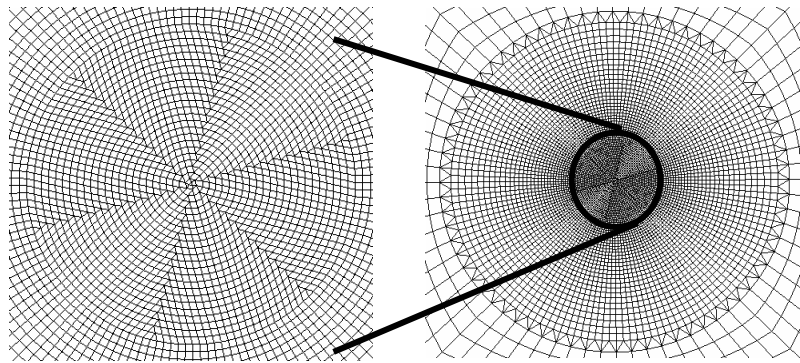


Figure 2.12. The center part (about 100 microns in diameter) of the thin film FEM element mesh used in the simulation.

The finite element simulations are performed using a commercial code, ABAQUS Standard Version 6.4.1 [19]. The elements used for modeling are 6 or 8 nodes 3D continuum elements (C3D8 and C3D6) in the thin film, which can model large deformation problems and provide high accuracy in problems involving contact. There are 14,007 nodes and 7338 elements in the thin film. The position of each node and the geometry shape of

each element are carefully designed to have nearly equal sides in lateral dimension in order to avoid irregularity, and this information is supplied in user-developed input files. The refined region covers the center area of the thin film with  $100\mu\text{m}$  in diameter. Within the refined region, the largest element is about  $5\mu\text{m} \times 5\mu\text{m}$ , and the smallest element size is  $0.5\mu\text{m} \times 0.5\mu\text{m}$ . The refined mesh is shown in figure 2.12 and the over all model including both the film and the indenter are shown in figure 2.13.

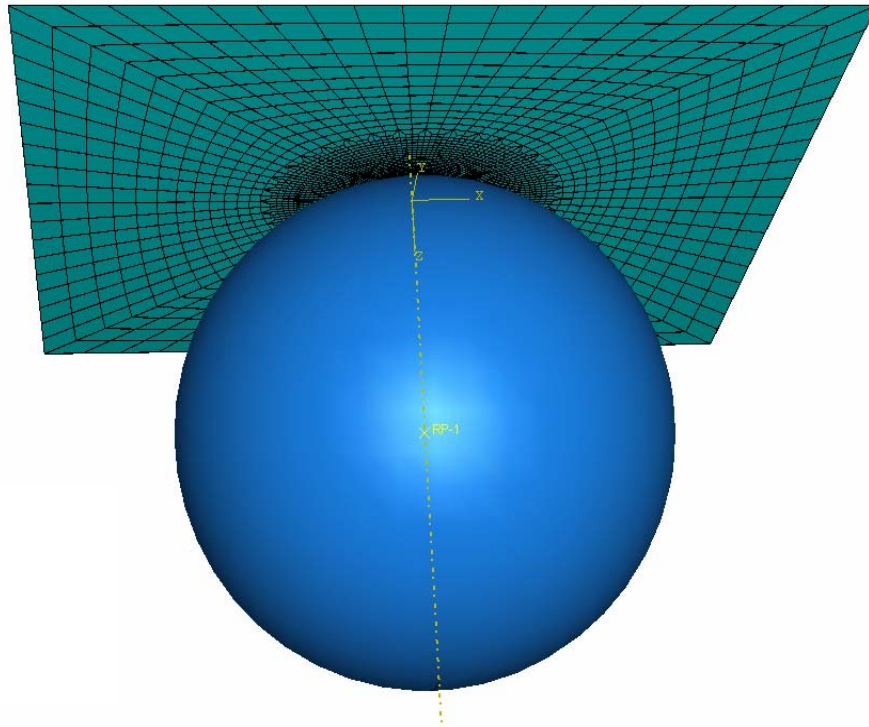


Figure 2.13. FEM mesh for the numerical simulation.

The user-developed modeling and analysis code uses a complete thin film and indenter geometry instead of part of it, thus no additional symmetry conditions is imposed.

The initial material properties for the thin film amorphous  $\text{Si}_3\text{N}_4$  are chosen to approximate the properties close to that of the bulk ceramic  $\text{Si}_3\text{N}_4$ . Accordingly, the elastic

modulus and the Poisson's ratio are chosen to be 300 GPa and 0.22, respectively [17]. The linear elastic material model (elastic constitutive model of ABAQUS) with large deformation capability is chosen based on the experiment observation where there is no hysteresis in the loading-unloading process as indicated by the load-displacement curves (figures. 2.9 and 2.10) and the film appeared intact without any cracks after loading when examined using a high magnification microscope. The equi-biaxial residual stress in the film is specified to 370 MPa in the simulations corresponding to the nominal value often found in the literature for this type of thin film [17].

To model the contact problem, the top surface of the film is defined as the slave surface and the spherical surface of the indenter as the master surface in the contact pair. Because both of the materials are ceramics which tend to have large adhesion and the high stress inside the film indicate that the contact pair could have very strong interaction. According to these reasons, rough surface interaction is assumed and the friction coefficient for the contact is set to be 0.8.

There are two ideal situations of surface interaction: frictionless and non-sliding with friction coefficient of 0 and 1 respectively. The situations in reality usually are combinations of these two cases. For typical indentation tests, which are different from normal friction related situation, "small sliding" interaction is selected with typical friction coefficient of 0.8.

The indentation displacement is increased monotonically to a maximum displacement of 50  $\mu\text{m}$  in 200 steps. This is much larger than the measured experimental displacement. The geometrically non-linear solver for large deformation in ABAQUS is employed for

solving the boundary value problem. At the end of each step, the stress component in the  $z$ -direction (vertical) of the indenter is integrated in the contact area to obtain the total indentation force. Thus, the force-center displacement curve is obtained.

### 2.4.1 Results

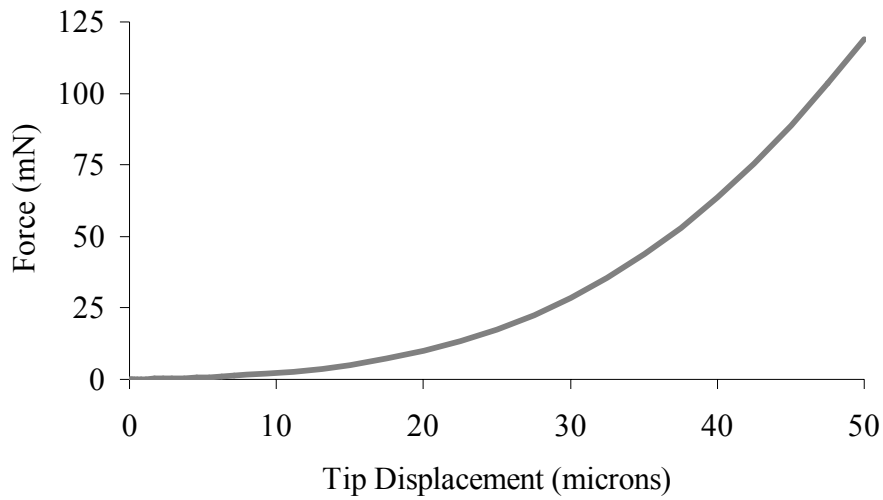


Figure 2.14. Load-deflection ( $F-d$ ) curve obtained from the finite element simulation and is used to obtain the shape factors in equation. (2.4). The solid curve is the fit and the solid dots are the finite element analysis data.

The load verses center-deflection curve ( $F-d$  curve) is shown in figure 2.14 for the geometrical and material parameters specified in the previous section. It is critical to choose the right form of the relation between the indentation force ( $F$ ) and the center displacement ( $d$ ). The solution to corresponding one-dimensional problem [18,19] indicates

that two terms should be included in the  $F-d$  relation: a linear term and a cubic term with respect to  $d$ . The linear term dominates the small deflection regime and is strongly affected by the residual stress. The cubic term dominates the large deflection regime is strongly influenced by the modulus of the material. The research on a square membrane under similar contact conditions still remains an open problem. However, it is reasonable to assume that the solution to the square membrane is similar to the circular membrane, except for coefficients (shape factors) to describe the shape difference effects.

Based on the arguments outlined above, the force-displacement ( $F-d$ ) relation is assumed to have the following form

$$F = C_1 at \left[ \sigma_0 \left( \frac{d}{a} \right) + C_2 \frac{E}{(1-\nu^2)} \left( \frac{d}{t} \right)^3 \right]. \quad (2.4)$$

The equation (2.4) can be rewritten in the following form

$$F = A_1 d + A_3 d^3, \quad (2.5)$$

where  $A_1$  and  $A_3$  are coefficients corresponding to the linear term and cubic term respectively. The least square fitting of the force-displacement  $F-d$  curve in fig 2.1 results in the coefficients,  $A_1 = 0.134 \text{ mN}/\mu\text{m}$  and  $A_3 = 9.047 \times 10^{-4} \text{ mN}/\mu\text{m}^3$ .

Then, for the assumed material properties in the finite element simulations,  $E = 300 \text{ GPa}$ ,  $\nu = 0.22$  and  $\sigma_0 = 370 \text{ MPa}$ , the two dimensionless coefficients  $C_1$  and  $C_2$  can be derived from the following equation as  $C_1 = 3.62$  and  $C_2 = 1.82 \times 10^{11}$ ,

$$C_1 = \frac{A_1}{t\sigma_0} \quad (2.6)$$

$$C_2 = \frac{A_3(1-\nu^2)t^2}{C_1 Ea} \quad (2.7)$$

$C_1$  and  $C_2$  are shape factors, which are independent of material. Therefore, the experimental sample with the same dimensions as the simulated one obeys eq. (2.4) with the same values of  $C_1$  and  $C_2$ . Using these parameters and the least square fitting coefficients from the experimental results for  $\text{Si}_3\text{N}_4$ , the elastic modulus and residual stress can be extracted. This will be explained in detail in the following section.

The finite element analysis was used to visualize the stress distribution inside the film. Figure 2.15 shows the displacement profile and figure 2.16 shows the maximum principle stress distribution for 30  $\mu\text{m}$  displacement of the indenter, which is similar to the experimental loading case. The stress visualization suggests that the film is subjected to large stress. Most of the film has the tensile equivalent stress between 1 GPa and 2 GPa. The stress is especially high inside the contact region, which reaches to 6.2 GPa. This is very similar to the estimated stress in previous section. However, for larger indenter displacement such as 40  $\mu\text{m}$ , the stress can be as large as 15 GPa, which is about 6% of the Young's modulus and at the same level as the theoretical strength. In this case, new mechanisms may occur to affect the mechanical behavior significantly. As a result, the linear elastic behavior will no longer be able to describe the phenomena. For this reason, data with indentation depth smaller than 35  $\mu\text{m}$  are used in the analysis thereafter. For a

membrane device under concentrated load in the center, not only the contact region but also the clamped edges need to be considered in designing from a reliability point of view.

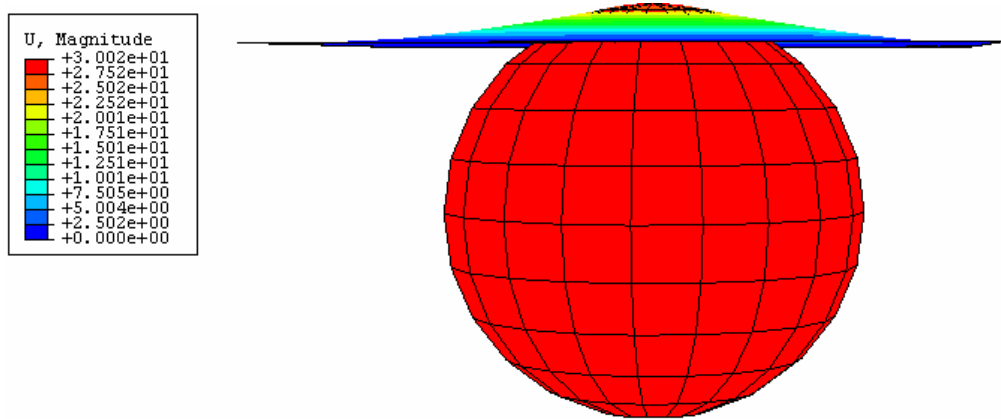


Figure 2.15. FEM result of displacement profile (side view).

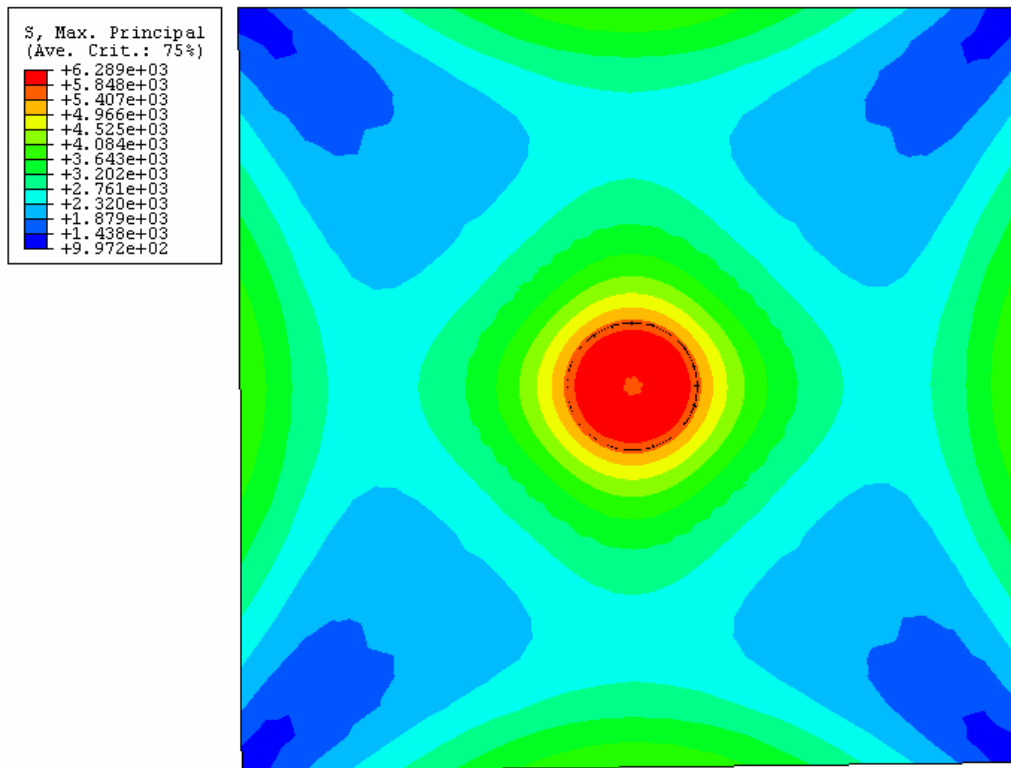


Figure 2.16. FEM result of distribution of maximum principle stress. Indentation displacement is 30 microns.

### 2.4.2 Mechanical properties analysis

Figure 2.17 shows the least square fitting of the experimental force-displacement ( $F-d$ ) curve. By fitting the  $F-d$  curve using equation (2.5), the fitting coefficients,  $A_1$  and  $A_3$ , can be obtained as  $A_1=0.123 \text{ mN}/\mu\text{m}$  and  $A_3=2.38 \times 10^{-4} \text{ mN}/\mu\text{m}^3$ .

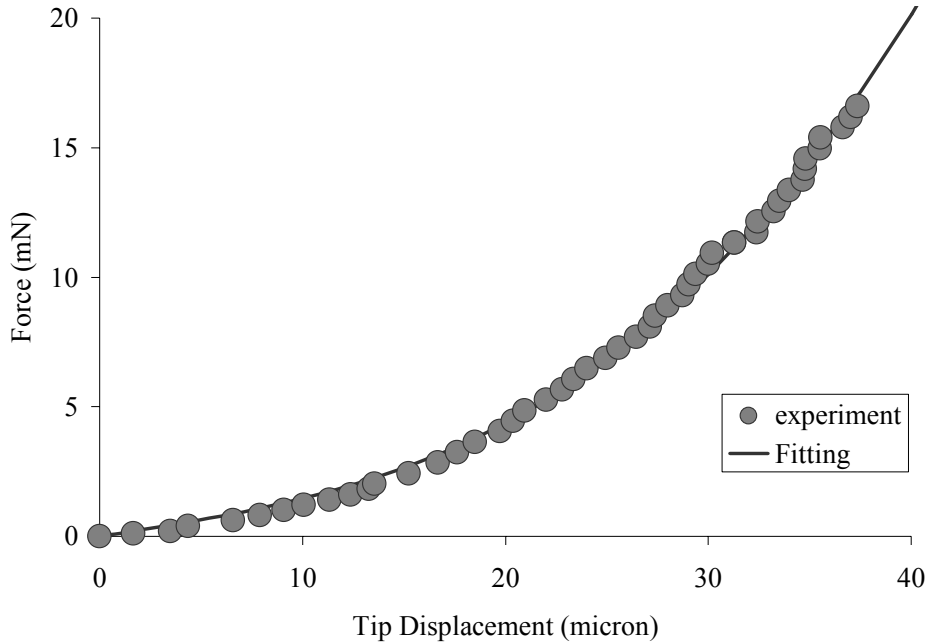


Figure 2.17. Least square fitting of force-displacement ( $F-d$ ) curve of the experimental data for extracting material properties using equations. (2.8) and (2.9).

From previous section, the dimensionless fitting parameters  $C_1$  and  $C_2$  are 3.62 and  $1.82 \times 10^{11}$ , respectively. Then, by using the following equations, the initial stress  $\sigma_0$  and the elastic modulus  $E$  in the thin film can be obtained as  $\sigma_0 = 451.5 \text{ MPa}$  and  $E = 248.2 \text{ GPa}$ ,

$$\sigma_0 = \frac{A_1}{C_1 t} \quad (2.8)$$

$$E = \frac{A_3(1-\nu^2)t^2}{C_1 C_2 a} \quad (2.9)$$

The above results, 248.2 GPa for Young's modulus and 451.5 MPa for residual stress, agree very well with the characterization results of the same sample by a different technique, pressure bulge test (see chapter 3 for more details). Compared with the Young's modulus of thin film  $\text{Si}_3\text{N}_4$  characterized by other group, these numbers are in very reasonable range.

The errors in the tests come from the displacement and the force measurements. Typical error from displacement measurements is about 0.1  $\mu\text{m}$  over the displacement range of 30  $\mu\text{m}$ , which is less than 1%. Errors in the force measurements include a 5% error from the load cell and a less-than 0.1% error from the micrometer. Therefore, the total error in the analysis is about 5.5%.

The  $F$ - $d$  curve is very sensitive to the values of Young's modulus  $E$  and residual stress  $\sigma_0$ . For a given  $F$ - $d$  curve, the fitted  $E$  and  $\sigma_0$  are unique.

## 2.5 Discussion

Thin film structures under transverse loading, whether distributed or concentrated can have either linear response or non-linear response. This means the center displacement ( $d$ ) versus the loading ( $F$ ) relationship is either linear or non-linear. For circular plates under

concentrated or pressure loading, a parameter  $\lambda$  has been used to determine the type of response.

$$\lambda = [12(1-\nu^2)]^{3/2} \left( \frac{Pa^2}{Eh^4} \right)$$

Table 2.1. Critical values of  $\lambda$  (adopted from reference 18).

	Clamped		Simply supported	
	Plate	Membrane	Plate	Membrane
Point loading	85	$3 \times 10^4$	20	$1 \times 10^4$
Pressure loading	300	$2 \times 10^3$	40	100

Critical values of  $\lambda = [12(1-\nu^2)]^{3/2} \left( \frac{Pa^2}{Eh^4} \right)$  plate/membrane response.

In our experiments,  $\lambda=10^8 \gg 10^3$ , which is the critical value for membrane behavior as shown in Table 2.1. Hence, the loading vs. maximum deflection curve should be expected to be non-linear. This was shown previously and the response is in agreement with theoretical predictions.

From equation (2.4), one can see that the pre-stress makes the film stiffer, i.e., for the loading with the same magnitude, the pre-stressed (tensile) film will have less center deflection. This feature can be used in MEMS devices to improve the performance. The pre-stress can be as much as several hundred MPa, and this can cause a difference in the center deflection as much as 20%, which can affect the performance of the MEMS devices significantly.

## 2.6 Conclusions

A new technique for the mechanical characterization of released thin films under concentrated load has been developed. This technique can be used to apply load in the  $\mu\text{N}$ – $\text{mN}$  range by either load control or displacement control. The displacement can be measured to high accuracy to within  $0.1\ \mu\text{m}$ . The capability and reliability of this new technique has been demonstrated by studying  $\text{Si}_3\text{N}_4$  free-standing membranes. The elastic modulus and residual stress of  $\text{Si}_3\text{N}_4$  free standing thin film are around 250 GPa and 400 MPa, respectively. These values are in close agreement with values obtained using a different technique and as well as those found in the literature. The significance of the residual stress in design and performance of MEMS devices is discussed.

## 2.7 References

1. S. D. Senturia, *Microsystem design*, (Kluwer Publishers, Boston 2001).
2. W. N. Sharpe, in *The MEMS Handbook*, edited by M. Gad-el-Hak (CRC Press, Boca Raton, FL 2001).
3. S. M. Spearing, *Acta Mater.*, **48**, 179-196 (2000).
4. V. T. Srikar, and S. M. Spearing, *Exp. Mech.*, **43**, 238-247 (2003).
5. M. A. Haque, and M. T. A. Saif, *Exp. Mech.*, **43(3)**, 248-255 (2003).
6. O. Kraft, and C. A. Volkert, *Adv. Eng. Mater.*, **3**, 99-110 (2001).
7. T. Y. Zhang, Y. J. Su, C. F. Qian, M. H. Zhao, and L. Q. Chen, "Microbridge testing of silicon nitride thin films deposited on silicon wafer", *Acta Mater.*, **48**, 2843-2857 (2000).

8. J. J. Vlassak, and W. D. Nix, *J. Mater. Res.*, **7**, 3242-3249 (1992).
9. D. T. Read, and J. W. Dally, *J. Mater. Res.*, **8(7)**, 1542–1549 (1993).
10. I. Chasiotis, and W. Knauss, *Exp. Mech.*, **42(1)**, (2002).
11. M. A. Haque, and M. T. A. Saif, *Exp. Mech.*, **42**, 123-128 (2002).
12. R. D. Emery, and G. L. Povirk, *Acta Mater.*, **51** 2067-2078 (2003); **51** 2079-2087 (2003).
13. H. D. Espinosa, B. C. Prorok, and M. Fischer, *J. Mech. Phys. Solids*, **51**, 47-67 (2003).
14. W. N. Sharpe, and D. S. Gianola, *Exp. Tech.*, **28**, 23-27 (2004).
15. J. A. Ruud, D. Josell, F. Spaepen, and A. L. Greer, *J. Mater. Res.*, **8(1)**, 112–117 (1993).
16. Y. Zhu, N. Moldova, and H. D. Espinosa, *Appl. Phys. Lett.*, **86**, 013506 (2005).
17. R. L. Edwards, and Sharpe, W.N., *Exp. Mech.*, **44**, 49-54 (2004). M. R. Begley, and T. J. Mackin, *J. Mech. Phys. Solids*, **52**, 2005–2023 (2004).
19. ABAQUS, [www.abaqus.com](http://www.abaqus.com).